Applied Catalysis B: Environmental 226 (2018) 46–52

Contents lists available at ScienceDirect

Applied Catalysis B: Environmental

journal homepage: www.elsevier.com/locate/apcatb

A novel route to synthesize C/Pt/TiO_2 phase tunable anatase–Rutile TiO_2 for efficient sunlight-driven photocatalytic applications

Chinh-Chien Nguyen, Duc Trung Nguyen, Trong-On Do*

Department of Chemical Engineering, Laval University, Québec, G1 V 0A6, Canada

ARTICLE INFO

Keywords:
Air-assisted carbon sphere combustion
Photocatalysts
Tunable anatase/rutile phase
Hydrogen production
Organic pollutant degradation

ABSTRACT

Herein, we report a novel air-assisted carbon sphere combustion process to produce phase-tunable anatase-rutile (A/R) C/Pt-TiO_2 photocatalysts for hydrogen generation and organic pollutant degradation under solar light irradiation. In the formed carbon/amorphous TiO_2 core/shell structure, the carbon-core was acted as a fuel to prepare the mixed phase A/R TiO_2 nanostructures. The A/R ratio of the TiO_2 nanoparticles was tuned by varying the purged air flow during the combustion process. The obtained materials exhibited several unique properties not achievable using conventional methods, including anatase/rutile homojunction, co-existence of C and Pt/PtO and very high surface area, significantly improved charge separation and transfer characteristics towards excellent photocatalytic properties. Eventually, the photocatalytic activities of the obtained materials were found to be more than 23 and 17 folds higher than commercial TiO_2-P25 for hydrogen generation and organic pollutant degradation, respectively.

1. Introduction

Since the first report by Fujishima and Honda in the late 20th century, the potential of inorganic semiconductor-based photocatalysts for the synthesis of renewable fuels and environmental remediation has been largely explored [1]. Despite their limited absorption in the UV region, TiO_2-based photocatalysts are the most investigated materials for photocatalytic applications owing to their extraordinary electronic properties, stability, eco-friendliness, and cost-effectiveness. Accordingly, considerable efforts have been rooted toward the synthesis of new TiO_2-based materials, several of which have demonstrated high efficiency for various applications [2–4]. Generally, TiO_2-based photocatalyst development has been focused on improvements in two areas: (i) development of TiO_2 as a visible-light-active photocatalyst and (ii) effective enhancement of the separation of excited electron/hole pairs in TiO_2. Significant efforts have been devoted toward the latter because insufficient charge separation is the predominant reason for limited photocatalytic activity in TiO_2 [5,6]. In this context, a controlled anatase–rutile (A/R) junction has proved to be a promising approach, as homo-junctions between different phases with the same chemical composition are expected to enhance charge separation, leading to significantly improve photoactivity [7–9]. For instance, the commercial photocatalyst TiO_2-P25 (Degussa-Huls) is composed of anatase and rutile phases and exhibits relatively good photocatalytic activity, which is associated with good charge separation at the interface of the rutile and anatase phases [10,11]. Recently, Ide et al. have reported the synthesis of a modified TiO_2 photocatalyst by hydrothermal treatment of commercial TiO_2-P25. This modified material showed enhanced photocatalytic efficiency several times as compared to initial TiO_2-P25 [12]. To this end, the preparation of TiO_2 nanoparticles with tunable ratios of coexisting A/R phases is highly desired. However, this task is conceptually challenging and the photocatalytic activity of commercial TiO_2-P25 remains limited because of insufficient charge separation, which could originate from (i) poor A/R homojunction, (ii) the absence of sufficiently active co-catalysts, or (iii) low specific surface area ($< 50\ m^2/g$). Hence, it is imperative to develop a novel, straightforward method for preparing efficient phase-tunable A/R TiO_2 photocatalysts. On the other hand, it is well known that colloidal carbon spheres can serve as hard templates for the preparation of materials with desired size- and shape-controlled properties, and can be removed easily upon calcination [13,14]. Interestingly, carbon spheres can also act as solid fuel for combustion to produce extremely high local temperature. Inspired by the above-mentioned unique features of the combustion process and carbon sphere templates, in this study, we developed an air-assisted carbon sphere combustion process (ACSC) using carbon spheres as a solid fuel and air flow, in which locally intense temperature inside the carbon sphere could be produced, to synthesize phase-tunable A/R TiO_2 nanoparticles. To the best of our knowledge, this is the first report of such a synthetic method.

* Corresponding author.
E-mail address: Trong-On.Do@gch.ulaval.ca (T.-O. Do).

https://doi.org/10.1016/j.apcatb.2017.12.038
Received 4 October 2017; Received in revised form 25 November 2017; Accepted 13 December 2017
Available online 15 December 2017
0926-3373/

2. Experimental

2.1. Chemicals

Glucose, hexachloroplatinic acid hexahydrate, and titanium isopropoxide were purchased from Aldrich. All reagents were used without further purification.

2.2. Synthesis of carbon colloidal spheres@Pt

Typically, 70 g of glucose was dissolved in 600 mL of deionized water. Next, 8 g of an aqueous solution of H_2PtCl_6 (1 mg/g) was added to this solution, which was then heated in a Teflon-lined autoclave at 180 °C for 18 h. Finally, the solid product was collected by centrifugation at 6000 ppm for 10 min, washed several times with water and ethanol, and dried overnight at 80 °C.

2.3. Synthesis of phase- tunable anatase–rutile C/Pt/TiO_2 (A/R)

As-prepared carbon colloidal spheres@Pt was coated with TiO_2 by hydrolysis of titanium isopropoxide on the carbon sphere surface. Briefly, 15 g of carbon colloidal spheres@Pt was dispersed in 500 mL of anhydrous ethanol and stirred for 2 h. Then, 15 g of an ethanol solution containing 1.2 g of titanium isopropoxide was slowly added into the solution, which was continuously stirred for 15 h. Next, the resulting material was recovered by centrifugation, washed with ethanol, and finally dried overnight at 80 °C in a vacuum oven. Subsequently, the resulting solid was subjected to carbon ignition by flame combustion. The combustion intensity was controlled using air at different flow rates.

2.4. Preparation of Pt-TiO_2 by conventional method

The photocatalysts prepared by conventional calcination method, denoted as Pt-TiO_2-CV, was obtained by calcination in air at 450 °C for 3 h from carbon colloidal spheres@Pt@TiO_2 to remove carbon colloidal spheres [15].

2.5. Preparation of Pt-TiO_2-P25

Samples of Pt supported on TiO_2-P25 was prepared by a photodeposition method [16,17]. Pt (2%) was photodeposited on the catalysts by dissolving H_2PtCl_6 in the reactant solution, followed by solar irradiation (150 W Xe lamp, AM 1.5 G, 100 mW cm^{-2}) of the solution for 4 h without the optical filter to facilitate Pt deposition.

2.6. Characterization

Transmission electron microscopy (TEM) images of the samples were recorded on a JEOL JEM 1230 system operated at 120 kV. Scanning electron microscopy (SEM) images were recorded on a JEOL 6360 system operated at 15 kV. Powder X-ray diffraction (XRD) patterns of the samples were recorded on a Bruker SMART APEX II XRD system equipped with a Cu Kα radiation source (λ = 1.5418 Å). X-ray photoelectron spectroscopy (XPS) measurements were carried out in the ion-pumped chamber (evacuated to 10^{-9} Torr) of a photoelectron spectrometer (Kratos Axis Ultra) equipped with a focused X-ray source (Al Kα, $h\nu$ = 1486.6 eV). UV–vis spectra were recorded on a Cary 300 Bio UV–vis spectrophotometer. N_2 adsorption-desorption isotherms were obtained at 77 K using a Quantachrome Autosorb-1 MP analyzer. Prior to measurements, the samples were outgassed under vacuum for 6 h at 150 °C. Photoluminescence (PL) measurements were carried out on a Cary Eclipse spectrofluorometer. The samples were excited at 340 nm. Carbon and Pt contents were obtained by elemental analysis using EAS1108, Fisons instruments and ICP-Ms (Agilent 8800), respectively.

2.7. Photocatalytic tests

2.7.1. Photocatalytic hydrogen production

Photocatalytic reactions of the composite photocatalysts were carried out in a top-down-type photoreactor connected to a closed-gas circulation system, as shown in Scheme S1. For the tests, 5 mg of photocatalyst was dispersed in 40 mL of a TEOA solution (10% w:w). Next, the suspension was thoroughly degassed with N_2 to remove air and irradiated using a solar simulator (Abet 103, 150 W Xe lamp, AM 1.5 G, 100 mW cm^{-2}), with an irradiance area of 4.5 cm^2 for 3 h. A water jacket was used to maintain the reactor temperature, which was stabilized at room temperature. The headspace volume is 20 mL, and the injected volume is 500 µL. The photocatalytic H_2 evolution rate was analyzed using an online Agilent gas chromatograph (GC, TCD detector, 5 Å molecular sieve columns, and N_2 carrier).

2.7.2. Photodecomposition of methanol

Photocatalytic reactions of the composite photocatalysts were carried out in a top-down-type photoreactor connected to a closed-gas circulation system, as shown in Scheme S1. An amount of photocatalyst (5 mg) was dispersed in 40 mL of a 5000 ppm solution of methanol in water. The reaction cell was then filled with fresh synthetic air (Prax air) and stirred for 1 h to reach the steady-state regime. Then, the cell was illuminated with a solar simulator (Abet 103, 150 W Xe lamp, AM 1.5 G, 100 mW cm^{-2}) for 3 h. The amount of CO_2 gas generated during the reaction was analyzed using a GC (Agilent 7820A) equipped with a TCD and HP-PLOT U column, with helium as the carrier gas. The headspace volume is 20 mL, and the injected volume is 500 µL.

2.7.3. Photocatalytic efficiency calculations

Photocatalytic efficiencies (PEs) were determined using solar simulator measurements [18,19]. The PEs were calculated using the number of photons needed to convert H_2O (or MeOH) to H_2 (or CO_2) for three hours is divided by the incident photons in the same period. The solar energy conversion was evaluated using an Abet solar simulator and C/Pt/TiO_2(A/R) as the light source and catalyst, respectively. Under full solar irradiation, the number of incident photons, calculated by integrating the intensity at each wavelength, was 2.75×10^{17} photon s^{-1} cm^{-2}, as shown in Fig. S7. A sample area of 4.5 cm^2 was irradiated for 3 h. Therefore, the number of incident photons was calculated as follows:

$$N_{\text{incidentphotons}} = (2.75 \times 10^{17}) \times 3 \times 4.5 \times 3600 = 1.3365 \times 10^{22} \text{ photons} \quad (1)$$

For hydrogen production, two photons are required to produce one H_2 molecule. After 3 h, the amount of H_2 generated under simulated solar light was determined as 49.5 µmol. Therefore, the number of photons consumed to produce H_2 molecules under solar light illumination over 3 h was calculated as follows:

$$N_{\text{consumedphotonsforH2}} = 49.5 \times 10^{-6} \times 2 \times 6.023 \times 10^{23} = 5.96 \times 10^{19} \quad (2)$$

$$\text{PE} = N_{\text{consumedphotonsforH2}}/N_{\text{incidentphotons}} = (5.96 \times 10^{19}/1.3365 \times 10^{22}) \times 100\% = 0.48\% \quad (3)$$

For CO_2 generation, the conversion of methanol (CH_3OH) to CO_2 was assumed to occur on C/Pt-TiO_2 (58/42) according to the following equation:

$$CH_3OH + H_2O + 6\,h^+ \rightarrow CO_2 + 6H^+ \quad (4)$$

The amount of CO_2 generated under simulated solar light was determined as 86.25 µmol and six photons are required to produce one CO_2 molecule. The corresponding number of photons consumed and PE

were calculated as follows:

$$N_{\text{consumedphotonsforCO2}} = 6 \times (86.25 \times 10^{-6}) \times (6.023 \times 10^{23}) = 3.116 \times 10^{20} \quad (5)$$

$$\text{PE} = N_{\text{consumedphotonsforCO2}}/N_{\text{incidentphotons}} = (3.116 \times 10^{20}/1.3365 \times 10^{22}) \times 100\% = 2.33\% \quad (6)$$

3. Results and discussion

Scheme S2 summarizes the three-step synthesis of the phase-tunable A/R TiO_2 nanoparticle material, abbreviated as C/Pt-TiO_2 (A/R). Initially, Pt supported carbon spheres were synthesized. Then, a core/shell structure with carbon spheres@Pt as the core and amorphous TiO_2 as the shell was prepared by coating titanium isopropoxide onto the surface of the carbon spheres. The resulting material, namely carbon spheres@Pt/TiO_2, was subjected to carbon ignition by combustion process. The air flow diffused into the system, leading to the intensive combustion of carbon- core and resulting in the formation of C/Pt-TiO_2 (A/R) due to highly intense combustion inside the core during the process. Because of the very high temperature inside the core and the high inertial forces acting on the TiO_2 walls, the implosive collapse of the core/shell structure occurred. As a result, the amorphous TiO_2 shell was converted into crystalline A/R TiO_2 in a short time (~360 s). Interestingly, it was found that the A/R phase ratio of the obtained TiO_2 material could be tuned by varying the rate of air flow in the system during the ACSC process.

It is important to note that the combustion step (Fig. 1A) was the most critical for achieving TiO_2 with tunable mixed A/R phases. When the carbon spheres@Pt/TiO_2, which is ignited by the flame, is subjected to the combustion under the air flow. Oxygen introduced by the air flow controlled the combustion intensity inside the carbon spheres. A higher air flow rate leads to a higher combustion intensity, which increases the temperature and pressure, facilitating the phase transformation of amorphous TiO_2 into A/R mixed phases. The combustion induced explosion of the materials could be found from photographic images as shown in Fig. 1B–D. The respective changes in the morphology of the material could be noticed in Fig. 1E and F, which show scanning electron microscopy (SEM) images of core/shell carbon spheres@Pt/TiO_2 and C/Pt-TiO_2 (A/R) before and after the combustion process. As seen in Fig. 1E, after loading TiO_2, reasonably uniform spheres with an approximate size of 500–700 nm were obtained. It should be noted that no significant change in the size and uniformity of the spheres was observed before and after coating with titanium isopropoxide. However, as shown in Fig. 1F, the air-flow-assisted combustion process induced significant changes in morphology. This change is likely due to the very high temperature inside the carbon spheres achieved in a short time, causing the implosive collapse of these spheres into nanoparticles with irregular sizes and shapes. This type of phase-tunable crystalline A/R TiO_2 cannot be achieved by conventional methods [20,21], such as

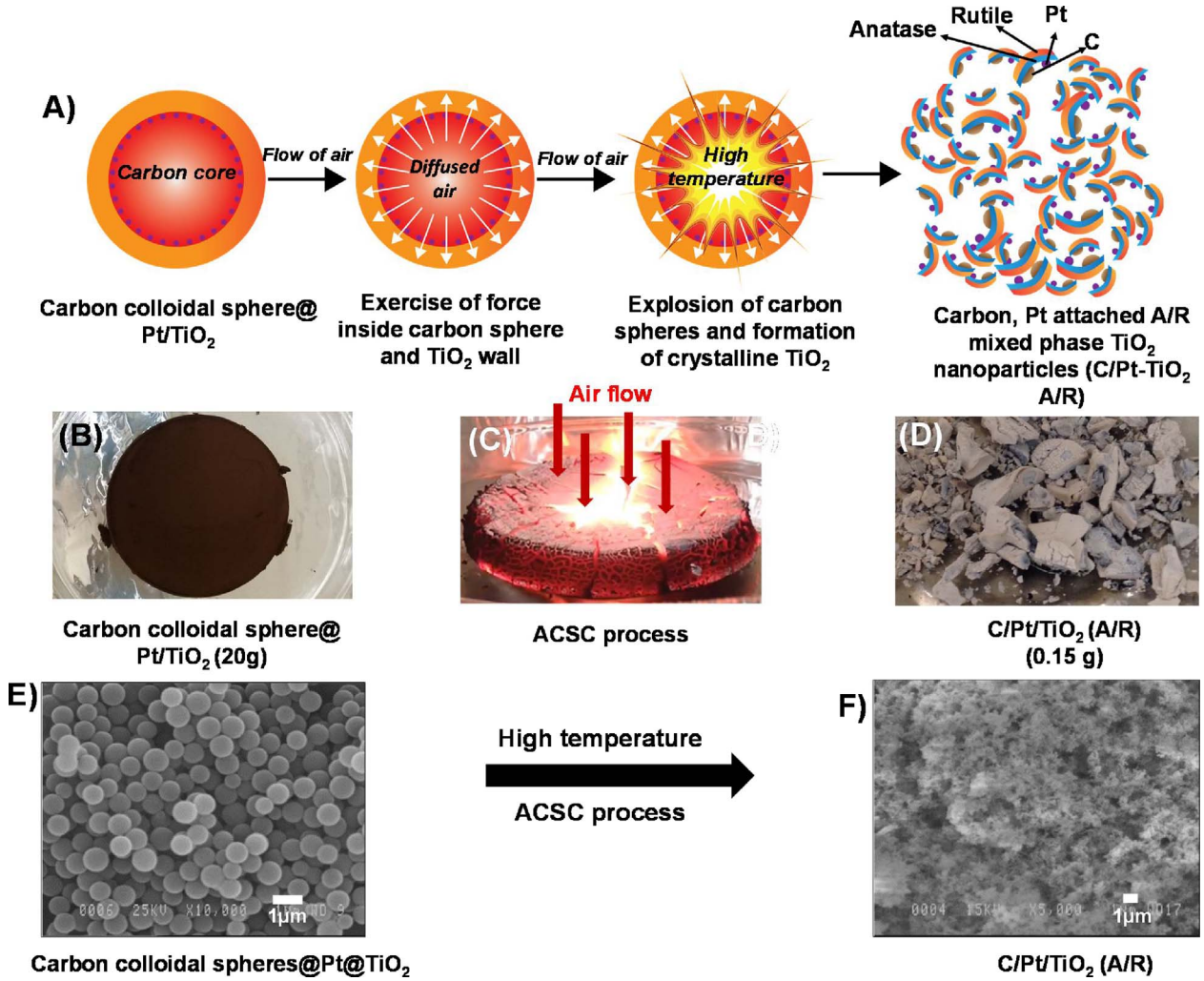

Fig. 1. A) Schematic representation of the air-assisted carbon sphere combustion (ACSC) process using carbon colloidal spheres as a solid fuel; B, C, and D) photographs of carbon colloidal spheres@Pt/TiO_2 before, during, and after ACSC process, respectively, corresponding to the preparation of C/Pt-TiO_2 (58/42); E and F) SEM images of colloidal carbon core/shell structures before and after the combustion process.

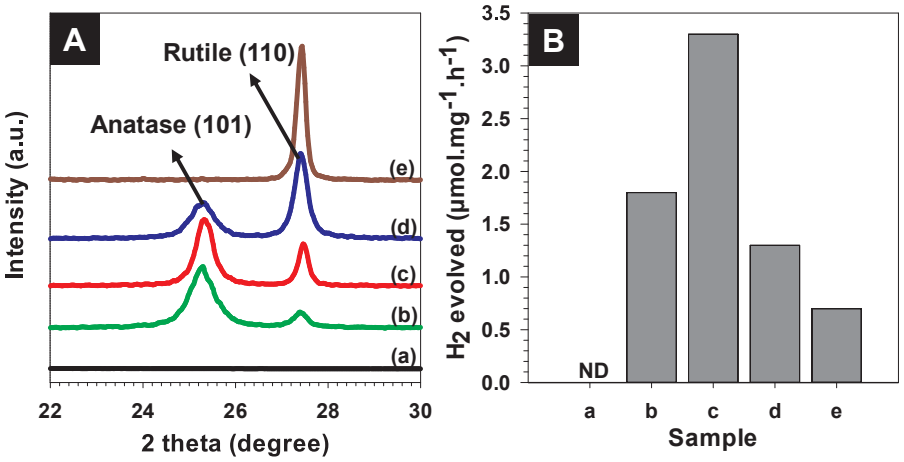

Fig. 2. A) XRD patterns of and B) photocatalytic hydrogen production by C/Pt-TiO_2 (A/R): A/R = a) 0/0, b) 79/21, c) 58/42, d) 40/60, and e) 0/100. ND: not determined.

sol–gel methods, where calcination at a high temperature (> 872 K) for several hours is required to obtain mixed A/R phases [22,23]. It can be seen that the attachment of carbon material with Pt-TiO_2 (A/R) nanostructures is essentially due to the combustion process and it is expected that the presence of carbon positively contributes to the overall photocatalytic activity of the material.

Fig. 2A shows X-ray diffraction (XRD) patterns of the samples before (line a) and after carbon sphere combustion, namely C/Pt-TiO_2 (A/R) (lines b–e) with different A/R ratios obtained by varying the air flow rate. For as-prepared carbon spheres@Pt/TiO_2 (line a), no XRD peaks were observed in the 2θ region of 22–30°, indicating that the sample before combustion consisted of amorphous TiO_2. However, after the ACSC process (lines b–e), peaks characteristic of TiO_2 anatase (A) and rutile (R) phases were observed in this region. As seen in Fig. 2A, the variation in the peak intensities (anatase (101) and rutile (110)) indicates the existence of A/R mixed phases with tunable ratios. Accordingly, the fraction of the rutile phase (FR) was calculated using $FR = I_R/(0.886I_A + I_R)$, where I_R and I_A are the integrated intensities of the anatase (101) and rutile (110) reflections, respectively [24]. As shown in Table S1, increasing FR along with decreasing carbon content were found with the increasing of air flow rate (from 50 to 500 mL/min), which indicates that higher air flow rates increase the temperature inside the carbon spheres, causing an implosive collapse in a short time and inducing rapid phase transformation from anatase to rutile. It should be noted that the rutile phase is only formed at temperatures higher than 873 K by conventional methods [25]. For the comparison, the XRD pattern of Pt-TiO_2-CV achieved by the conventional calcination method was shown in Fig. S1. It can be seen that rutile is a minor phase, for which the FR values were found to be 0.17. This indicates the high temperature resulted by the ACSC process, which could promote the phase transformation from anatase to rutile. Hence, the carbon colloidal spheres not only function as a template but also as a solid fuel to provide sufficient heat to the system for the anatase to rutile phase transformation under controlled air flow. Fig. 2B shows the photocatalytic activities of these samples for hydrogen generation under solar light irradiation. The best performance was achieved for the sample with 58% anatase and 42% rutile phases. The observation of the highest photocatalytic activity at this A/R ratio may be attributable to enhanced charge separation at the A/R interface [26]. Hence, this sample, namely C/Pt-TiO_2 (58/42), was selected for further characterization to understand its unique properties and photocatalytic mechanism.

Fig. 3 shows the structural and chemical state characteristics of C/Pt-TiO_2 (58/42), as obtained using XRD, Raman spectroscopy, and X-ray photoelectron spectroscopy (XPS). As seen in the XRD pattern in Fig. 3A (see also Fig. 2A-line c), both rutile and anatase phases are present in this sample. However, no XRD peaks corresponding to Pt are observed, indicating the fine dispersion of Pt nanoparticles in the C/TiO_2 (58/42) sample. Raman and UV–vis spectroscopy were employed to confirm the presence of carbon and mixed A/R TiO_2 phases in this sample [27,28]. As shown Fig. 3B, the Raman spectrum of C/Pt-TiO_2 (58/42) exhibits two distinct bands at 1360 and 1590 cm^{-1} corresponding to the D band, which is attributed to the vibration of carbon atoms in the amorphous carbon structure, and the G band, which is attributed to the vibration of sp^2-bonded graphitic carbon atoms in the carbon lattice, respectively [29]. Furthermore, the bands at 395, 515, and 636 cm^{-1} are characteristic of the anatase phase, whereas the bands at 446 and 609 cm^{-1} correspond to the vibrational modes of the rutile phase. These results are in good agreement with XRD analysis of the anatase and rutile phases [30,31].

It should be noted that a small amount of carbon residue (~4.5%) was found in the sample after the combustion process. Therefore, to study the optical properties of this material with and without carbon, the C/Pt-TiO_2 (58/42) sample was further calcined at 550 °C in air to remove the carbon residue. Fig. S2 shows the UV–vis spectra of C/Pt-TiO_2 (58/42) before and after calcination in air at 550 °C (abbreviated as Pt-TiO_2 (58/42)-550). For C/Pt-TiO_2 (58/42), a broad absorption band at 400–700 nm corresponds to the presence of carbon species [32] and this band is absent in the UV–vis spectrum of Pt-TiO_2 (58/42)-550. The origin of the emergence of this broad absorption band in C/Pt-TiO_2 (58/42) could be attributed to the increase of electric surface charge due to the carbon residue in the nanocomposite. This can positively influence the separation of electron-hole pairs in the material upon light irradiation [33,34,35]. In addition, as shown in Fig. S3, the XRD patterns of C/Pt-TiO_2 (58/42) before and after calcination in air at 550 °C indicate the calcination tempertature and the carbon residue do not affect the lattice composition and crystalline quality of TiO_2 phase in the composite.

X-ray photoelectron spectroscopy measurements were carried out to understand the chemical oxidation states of the elements in the obtained material. The survey spectrum of C/Pt-TiO_2 (58/42) (Fig. S4) confirmed the presence of C, Pt, and TiO_2 in the sample. The amount of C and Pt was estimated to be around 3.5 and 1.8 wt%, respectively, which was also confirmed by elemental and inductively coupled plasma (ICP-MS) analysis (3.42 and 1.8 wt%, respectively). In the Ti2p XPS spectrum of C/Pt-TiO_2 (58/42), the two peaks centered at binding energies of 459.28 and 464.99 eV, corresponding to $Ti2p_{3/2}$ and $Ti2p_{1/2}$, respectively, indicate the Ti^{4+} state of titanium in TiO_2 (Fig. S5) [36,37]. For the C1 s XPS spectrum of C/Pt-TiO_2 (58/42), as shown in Fig. 3C, three peaks centered at 285.0, 286.63, and 289.34 eV were found. The peak at 285.0 eV corresponds to sp^2 C—C, whereas those at 286.6 and 289.3 eV correspond to C—O and O—C=O, respectively [38]. Fig. 3D shows the Pt4f XPS spectrum of C/Pt-TiO_2 (58/42) where the two peaks centered at 71.09 and 74.42 eV correspond to $Pt4f_{7/2}$ and $Pt4f_{5/2}$ of Pt(0); however, the peaks at 72.49 and 75.82 eV correspond

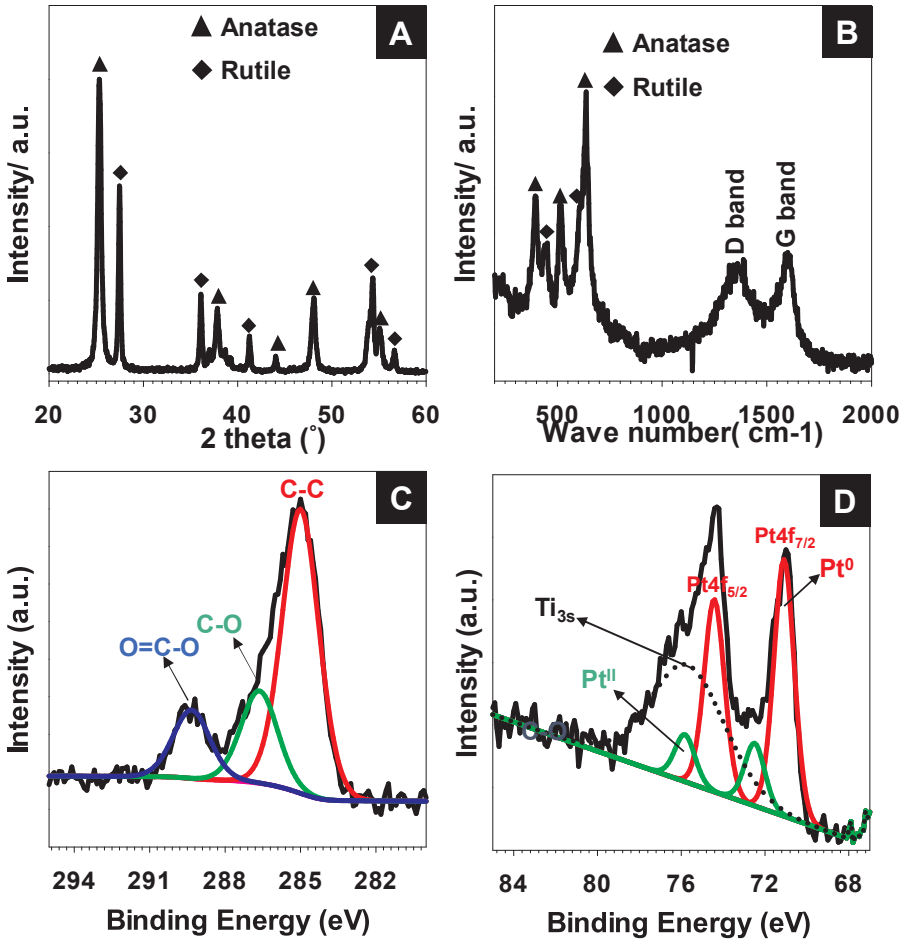

Fig. 3. A) XRD pattern, B) Raman spectrum, C) C1s XPS spectrum, and D) Pt4f XPS spectrum of C/Pt-TiO_2 (58/42).

to $Pt4f_{7/2}$ and $Pt4f_{5/2}$ of Pt(II), respectively [39,40]. The broad XPS peak at 75.7 eV corresponds to the satellite signal of Ti3 s [41]. The coexistence of Pt(II) (as PtO) with Pt(0) (as metallic Pt) is interesting property as it is expected to significantly enhance the photocatalytic performace of the nanocomposite [42–45].

Fig. 4A shows a transmission electron microscopy (TEM) image of C/Pt-TiO_2 (58/42) indicating TiO2 nanoparticles in the size range of 20–30 nm. The corresponding selected-area electron diffraction (SAED) pattern (Fig. 4A, inset) indicates the presence of A/R mixed phases in the sample. In addition, the high-resolution TEM (HR-TEM) image and fast Fourier transform (FFT) image in Fig. 4B clearly confirm the presence of A/R homojunction, with lattice spacing values of 3.5 and 3.2 Å corresponding to anatase (101) and rutile (110), respectively. The coexistence of C and Pt on TiO_2, as well as a heterojunction between Pt/TiO_2 and C/TiO_2, was confirmed by HR-TEM-energy-dispersive X-ray (EDX) analysis, as shown in Fig. 4C and D, and S6.

The photocatalytic activities of the C/Pt-TiO_2 (58/42) sample for hydrogen generation and methanol decomposition under solar light irradiation were evaluated, and the obtained results are given in Fig. 5.The power spectrum of simulated solar light was shown in Fig. S7. For comparison, Pt-TiO_2 (58/42)-550, Pt-TiO_2-P25 and Pt-TiO_2-CV with the same Pt loading were also studied under identical photocatalytic conditions, as shown in Table S2. The TEM images and corresponding XPS Pt spectra of these samples are shown in Fig. S8. It can be seen that only metallic Pt was observed for the sample Pt-TiO_2-P25 and Pt-TiO_2-CV, respectively whereas Pt(0), Pt^{II}(PtO) and Pt^{IV}(PtO_2) were found with the sample Pt-TiO_2(58/42)-550 indicating the further oxidation of Pt under annealing process [46,47]. As seen in Fig. 5A, C/Pt-TiO_2 (58/42) generated 3.3 mmol g^{-1} h^{-1} of H_2 which is approximately 41, 23 and 7 times higher than the amounts generated by Pt-TiO_2-CV, Pt-TiO_2-P25 and Pt-TiO_2 (58/42)-550, respectively. Thus, this C/Pt-TiO_2 (58/42) photocatalyst is among the very few TiO_2-based catalysts that exhibit significant photocatalytic activity under solar light (Table S3). Furthermore, regarding the methanol decomposition (Fig. 5B), ~5.7 mmol g^{-1} h^{-1} of CO_2 was formed using C/Pt-TiO_2 (58/42) under solar light, which is approximately 38, 17, and 5 times greater those of Pt-TiO_2-CV, Pt-TiO_2-P25 and Pt-TiO_2 (58/42)-550, respectively. Moreover, the sample C/Pt-TiO_2 (58/42) also showed the stability over 5 cycles as shown in Fig. S9. The photocatalytic efficiencies of C/Pt-TiO_2 (58/42) for hydrogen and CO_2 formation were calculated to be 0.48% and 2.33%, respectively under full solar light irradiation, which are relatively high values for TiO_2-based photocatalysts reported to date. The photocatalytic activities under UV light (254 nm) was also performed, as shown in Fig. S10. The amount of H_2 produced by C/Pt-TiO_2 (58/42) is 0.5 mmol g^{-1} h^{-1}, which is the significantly higher than those of Pt-TiO_2-CV, Pt-TiO_2-P25 and Pt-TiO_2 (58/42)-550, respectively. Similarly, C/Pt-TiO_2 (58/42) produced 0.8 mmol g^{-1} h^{-1} of CO_2, which is approximately 16, 7 times higher than those of Pt-TiO_2-CV and Pt-TiO_2-P25. This indicates the feature properties of C/Pt-TiO_2 (58/42) inducing by the ACSC process, which could not be obtained by the conventional methods.

To understand the mechanism responsible for the enhanced photocatalytic activity of C/Pt-TiO_2 (58/42), the characteristics of the surface texture of the structure were also studied. As catalytic performance strongly depends on the number of exposed light absorption and active sites on the catalyst surface, very high specific surface areas are required. Accordingly, the specific surface area of C/Pt-TiO_2 (58/42) was estimated to be 220 m^2 g^{-1}, which is approximately 5 and 4 times higher than those of Pt-TiO_2-CV (43 m^2 g^{-1}) and Pt-TiO_2-P25 (50 m^2 g^{-1}), respectively. It is also higher than those of TiO_2-based

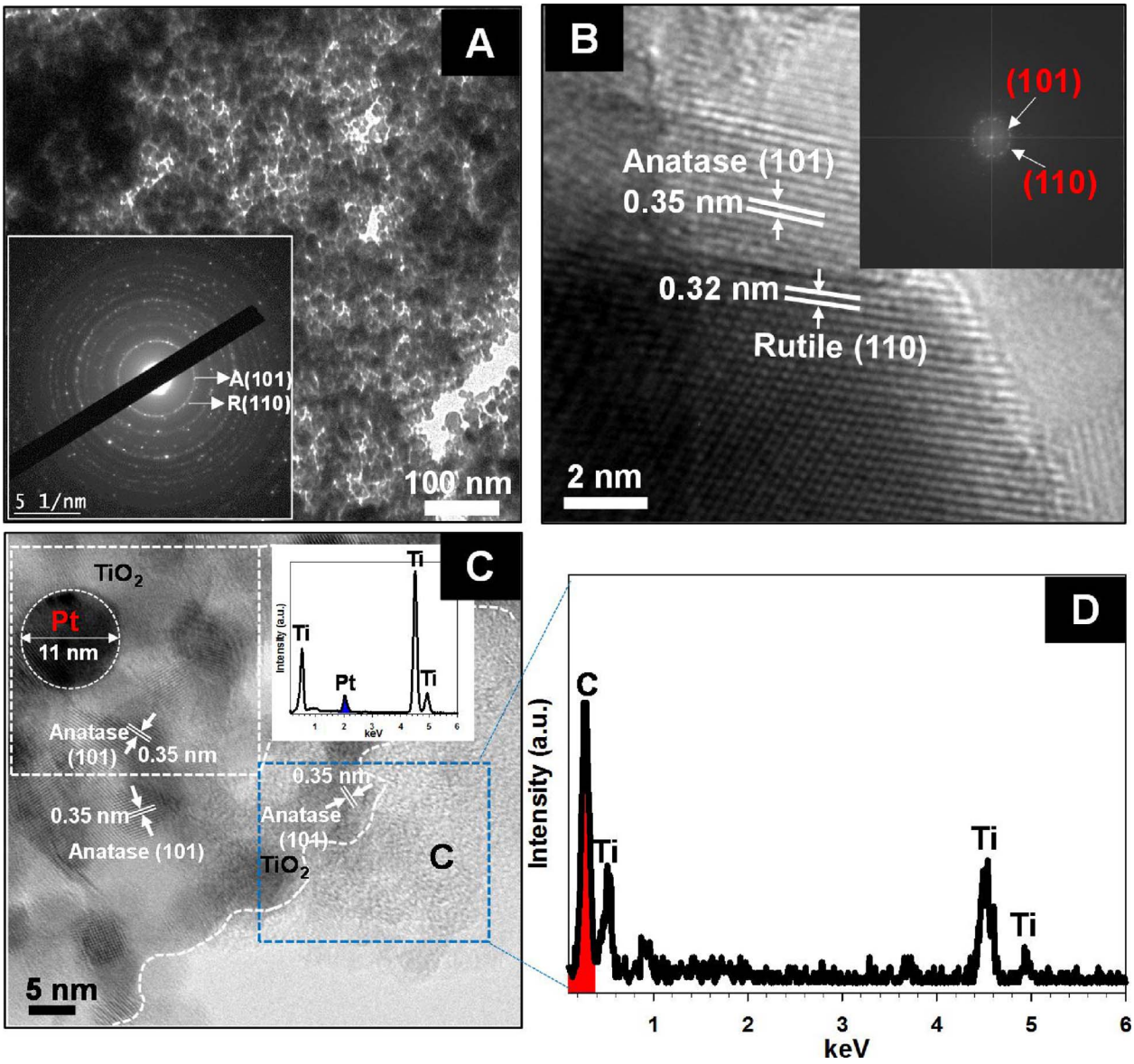

Fig. 4. A) TEM image with inset SAED pattern, B) HR-TEM image with inset FFT image, and C and D) HR-TEM-EDX analysis of C/Pt-TiO_2 (58/42).

photocatalysts prepared by other synthesis methods (Table S4). This indicates that the presence of carbon under the ACSC process could hinder the sintering effect. Furthermore, even the C/Pt-TiO_2 (58/42) sample was followed by calcination at higher temperatures, resulting in a higher specific surface area material (Pt-TiO_2 (58/42)-550, 320 $m^2 g^{-1}$). The adsorption/desorption isotherm of C/Pt-TiO_2 (58/42)

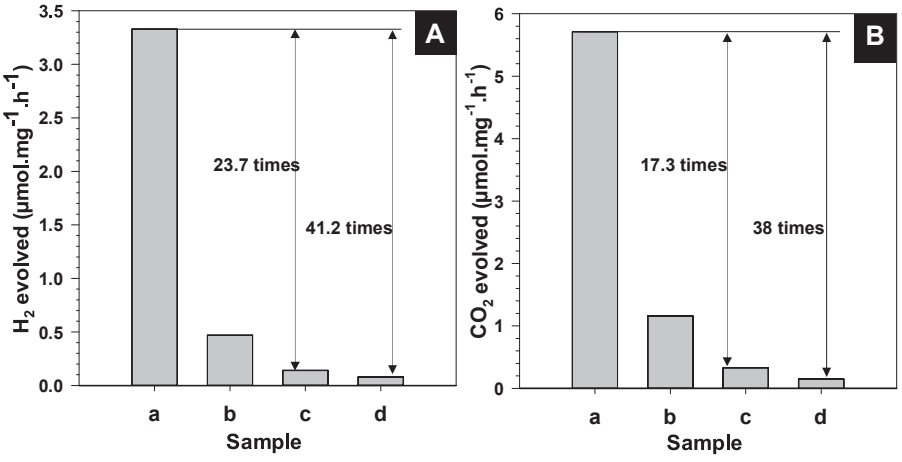

Fig. 5. (A) Hydrogen produced from water and (B) CO_2 produced by methanol degradation using a) C/Pt-TiO_2 (58/42), b) Pt-TiO_2 (58/42)-550, c) Pt-TiO_2-P25 and d) Pt-TiO_2-CV.

exhibited higher adsorption capacity at higher pressures, indicating a significant pore volume (Fig. S11A) [48]. The pore size distribution for C/Pt-TiO_2 (58/42) (Fig. S11B) calculated by the BJH method was in the range of 4–14 nm. High specific surface areas and large pore size facilitate mass transfer and efficiently accelerate photocatalytic reactions [49,50]. Interestingly, although the specific surface area of C/Pt-TiO_2 (58/42) (220 $m^2 g^{-1}$) was smaller than that of Pt-TiO_2 (58/42)-550 (320 $m^2 g^{-1}$), the photocatalytic activity of C/Pt-TiO_2 (58/42) was considerably higher than that of the calcined sample. This finding again indicates that co-existence of carbon and Pt/PtO in C/Pt-TiO_2 (58/42) has an important role and significantly contributes to charge separation in the nanocomposite. The separation efficiency of photoinduced electron-hole pairs was also demonstrated by steady-state photoluminescence (PL) measurements, as shown in Fig. S12. Compared to the PL intensity of Pt-TiO_2-P25, Pt-TiO_2-CV and Pt-TiO_2 (58/42)-550, a significantly reduced PL intensity was observed for C/Pt-TiO_2 (58/42), confirming the suppression of charge recombination in this sample. It is noteworthy that efficient charge separation in the sample necessarily increases the number of carriers available for photocatalytic reactions. This result is consistent with those reported for carbon-modified TiO_2 in which carbon has the mediating role in storing and shuttling photogenerated electrons from the semiconductor to an acceptor in a photocatalytic process [33]. Moreover, the co-existence of PtO with Pt also contributes to improve the photocatalytic performances by promoting the reduction photoreactions (e.g., $2H^+ \rightarrow H_2$) while suppressing back reactions (e.g., $H_2 \rightarrow 2H^+$), which are also catalyzed by Pt metal [45,51]. Consequently, the synergetic effect of these feature properties on C/Pt-TiO_2 (58/42) induced the high photocatalytic activities for both H_2 production and methanol degradation reaction under either solar or UV irradiation.

Based on the obtained results, the significantly improved photoactivity of C/Pt-TiO_2 (58/42) could be associated with the following three factors: (i) A/R homojunction, which significantly reduces the possibility of charge recombination [52]; (ii) C and Pt/PtO are attributed to enhance charge separation, supress back reactions and promote photoreactions; and (iii) a high surface area and large pore volume can enhance the exposed light absorption (TiO_2 A/R) and active sites (C and Pt/PtO) for the photocatalytic reaction as well as the adsorption of water and methanol molecules onto the surface, as shown in Fig. S13.

4. Conclusions

In summary, a new approach was developed for the preparation of efficient C/Pt-TiO_2 (A/R) mixed phase photocatalysts using the ACSC process. The A/R ratio of TiO_2 was tunable by varying the air flow during carbon sphere combustion. The C/Pt-TiO_2 (58/42) sample exhibited unique properties, which could not be found by the other conventional methods, inducing the synergistic effect to boost the photocatalytic activities under solar light irradiation. Further studies focusing on a detailed understanding of the formation of mixed A/R phases are underway in our laboratory. We believe that this approach opens a new avenue for the development of efficient photocatalysts and other catalytic systems.

Acknowledgements

This work was supported by the Natural Science and Engineering Research Council of Canada (NSERC) through Collaborative Research and Development (CRD), Strategic Project (SP), and Discovery Grants. The authors would like to thank Exp Inc. and SiliCycle Inc. for their support and Dr. Sakar Mohan for his helpful discussion.

Appendix A. Supplementary data

Supplementary data associated with this article can be found, in the online version, at https://doi.org/10.1016/j.apcatb.2017.12.038.

References

[1] X. Chen, S. Shen, L. Guo, S.S. Mao, Chem. Rev. 110 (2010) 6503–6570.
[2] H. Park, H.-I. Kim, G.-H. Moon, W. Choi, Energy Environ. Sci. 9 (2016) 411–433.
[3] J.J. Brancho, B.M. Bartlett, Chem. Mater. 27 (2015) 7207–7217.
[4] J. Matos, T. Marino, R. Molinari, H. García, Appl. Catal. A (2012) 263–272.
[5] X. Liu, G. Zhu, X. Wang, X. Yuan, T. Lin, F. Huang, Adv. Energy Mater. 6 (2016) 1600452.
[6] M. Nolan, A. Iwaszuk, A.K. Lucid, J.J. Carey, M. Fronzi, Adv. Mater. (2016) 5425–5446.
[7] D.O. Scanlon, C.W. Dunnill, J. Buckeridge, S.A. Shevlin, A.J. Logsdail, S.M. Woodley, C.R.A. Catlow, M.J. Powell, R.G. Palgrave, I.P. Parkin, Nat. Mater. 12 (2013) 798–801.
[8] S. Shen, X. Wang, T. Chen, Z. Feng, C. Li, J. Phys. Chem. C 118 (2014) 12661–12668.
[9] Y. Gao, J. Zhu, H. An, P. Yan, B. Huang, R. Chen, F. Fan, C. Li, J. Phys. Chem. Lett. 8 (2017) 1419–1423.
[10] T. Ohno, K. Sarukawa, K. Tokieda, M. Matsumura, J. Catal. 203 (2001) 82–86.
[11] D.C. Hurum, A.G. Agrios, K.A. Gray, T. Rajh, M.C. Thurnauer, J. Phys. Chem. B 107 (2003) 4545–4549.
[12] Y. Ide, N. Inami, H. Hattori, K. Saito, M. Sohmiya, N. Tsunoji, K. Komaguchi, T. Sano, Y. Bando, D. Golberg, Angew. Chem. Int. Ed. 55 (2016) 3600–3605.
[13] X. Sun, Y. Li, Angew. Chem. Int. Ed. 43 (2004) 3827–3831.
[14] C.C. Nguyen, N.N. Vu, T.-O. Do, J. Mater. Chem. A 3 (2015) 18345–18359.
[15] W. Shen, Y. Zhu, X. Dong, J. Gu, J. Shi, Chem. Lett. 34 (2005) 840–841.
[16] G.R. Bamwenda, S. Tsubota, T. Nakamura, M. Haruta, J. Photochem. Photobiol. A Chem. 89 (1995) 177–189.
[17] T. Abe, E. Suzuki, K. Nagoshi, K. Miyashita, M. Kaneko, J. Phys. Chem. B 103 (1999) 1119–1123.
[18] S.E. Braslavsky, A.M. Braun, A.E. Cassano, A.V. Emeline, M.I. Litter, L. Palmisano, V.N. Parmon, N. Serpone, Pure Appl. Chem. 83 (2011) 931–1014.
[19] M. Liu, X. Qiu, M. Miyauchi, K. Hashimoto, J. Am. Chem. Soc. 135 (2013) 10064–10072.
[20] C.-C. Nguyen, N.-N. Vu, T.-O. Do, J. Mater. Chem. A 4 (2016) 4413–4419.
[21] A. Ivanova, M.C. Fravventura, D. Fattakhova-Rohlfing, J. Rathousky, L. Movsesyan, P. Ganter, T.J. Savenije, T. Bein, Chem. Mater. 27 (2015) 6205–6212.
[22] L. Cao, D. Chen, W. Li, R.A. Caruso, ACS Appl. Mater. Interfaces 6 (2014) 13129–13137.
[23] Z. Luo, A.S. Poyraz, C.-H. Kuo, R. Miao, Y. Meng, S.-Y. Chen, T. Jiang, C. Wenos, S.L. Suib, Chem. Mater. 27 (2014) 6–17.
[24] F. Xu, W. Xiao, B. Cheng, J. Yu, Int. J. Hydrog. Energy 39 (2014) 15394–15402.
[25] T.A. Kandiel, L. Robben, A. Alkaim, D. Bahnemann, Photochem. Photobiol. Sci. 12 (2013) 602–609.
[26] R. Su, R. Bechstein, L. Sø, R.T. Vang, M. Sillassen, B.R. Esbjörnsson, A. Palmqvist, F. Besenbacher, J. Phys. Chem. C 115 (2011) 24287–24292.
[27] M.A. Pimenta, G. Dresselhaus, M.S. Dresselhaus, L.G. Cancado, A. Jorio, R. Saito, Phys. Chem. Chem. Phys. 9 (2007) 1276–1290.
[28] L. Li, J. Yan, T. Wang, Z.-J. Zhao, J. Zhang, J. Gong, N. Guan, Nat. Commun. 6 (2015).
[29] L. Yu, G. Li, X. Zhang, X. Ba, G. Shi, Y. Li, P.K. Wong, J.C.M. Yu, Y. Yu, ACS Catal. (2016) 6444–6454.
[30] M.S.P. Francisco, V.R. Mastelaro, Chem. Mater. 14 (2002) 2514–2518.
[31] A. Li, Z. Wang, H. Yin, S. Wang, P. Yan, B. Huang, X. Wang, R. Li, X. Zong, H. Han, C. Li, Chem. Sci. 7 (2016) 6076–6082.
[32] S. Sakthivel, H. Kisch, Chem. Int. Ed. 42 (2003) 4908–4911.
[33] L.W. Zhang, H.B. Fu, Y.F. Zhu, Adv. Funct. Mater. 8 (2008) 2180–2189.
[34] J. Zhong, F. Chen, J. Zhang, J. Phys. Chem. C 114 (2010) 933–939.
[35] M. Wang, J. Han, Y. Hu, R. Guo, Y. Yin, ACS Appl. Mater. Interfaces 8 (2016) 29511–29521.
[36] Y. Yang, G. Liu, J.T.S. Irvine, H.-M. Cheng, Adv. Mater. 28 (2016) 5850–5856.
[37] J. Hu, L. Wu, K.A. Kuttiyiel, K.R. Goodman, C. Zhang, Y. Zhu, M.B. Vukmirovic, M.G. White, K. Sasaki, R.R. Adzic, J. Am. Chem. Soc. 138 (2016) 9294–9300.
[38] S. Zhu, Q. Meng, L. Wang, J. Zhang, Y. Song, H. Jin, K. Zhang, H. Sun, H. Wang, B. Yang, Angew. Chem. Int. Ed. 52 (2013) 3953–3957.
[39] Y. Miseki, S. Fujiyoshi, T. Gunji, K. Sayama, Catal. Sci. Tech. 3 (2013) 1750–1756.
[40] G. Zhang, Z.-A. Lan, L. Lin, S. Lin, X. Wang, Chem. Sci. 7 (2016) 3062–3066.
[41] M.F. Finol, J. Rooke, B.-L. Su, M. Trentesaux, J.-M. Giraudon, J.-F. Lamonier, Catal. Today 92 (2012) 154–159.
[42] R. Abe, M. Higashi, K. Domen, ChemSusChem 4 (2011) 228–237.
[43] S.R. Shin, J.H. Park, K.-H. Kim, K.M. Choi, J.K. Kang, Chem. Mater. 28 (2016) 7725–7730.
[44] Y. Hang Li, J. Xing, Z. Jia Chen, Z. Li, F. Tian, L. Rong Zheng, H. Feng Wang, P. Hu, H. Jun Zhao, H. Gui Yang, Nat. Commun. 4 (2013) 2500.
[45] N.R. Manwar, A.A. Chilkalwar, K.K. Nanda, Y.S. Chaudhary, J. Subrt, S.S. Rayalu, N.K. Labhsetwar, ACS Sustain. Chem. Eng. 4 (2016) 2323–2332.
[46] E.I. Vovk, A.V. Kalinkin, M.Y. Smirnov, I.O. Klembovskii, V.I. Bukhtiyarov, J. Phys. Chem. C 121 (2017) 17297–17304.
[47] M. Sarno, E. Ponticorvo, Int. J. Hydrog. Energy 42 (2017) 23631–23638.
[48] J. Zhang, J. Yu, Y. Zhang, Q. Li, J.R. Gong, Nano Lett. 11 (2011) 4774–4779.
[49] Q. Liang, Z. Li, Z.H. Huang, F. Kang, Q.H. Yang, Adv. Funct. Mater. (2015) 6885–6892.
[50] T. Weller, J. Sann, R. Marschall, Adv. Energy Mater. 6 (2016) 1600208.
[51] J. Kiwi, M. Grätzel, Angew. Chem. Int. Ed. 17 (1978) 860–861.
[52] X. Sun, W. Dai, G. Wu, L. Li, N. Guan, M. Hunger, Chem. Commun. 51 (2015) 13779–13782.